NASA CONTRACTOR REPORT 181840

TREATMENT OF SINGULARITIES IN CRACKED BODIES

K. N. SHIVAKUMAR AND I. S. RAJU

ANALYTICAL SERVICES AND MATERIALS, INC.
Hampton, VA 23666

Contract NAS1-18599

MAY 1989

National Aeronautics and
Space Administration

Langley Research Center
Hampton, Virginia 23665-5225

SUMMARY

Three-dimensional finite-element analyses of middle-crack tension (M-T) and bend specimens subjected to mode I loadings were performed to study the stress singularity along the crack front. The specimen was modeled using 20-node isoparametric elements with collapsed, non-singular elements at the crack front. The displacements and stresses from the analysis were used to estimate the power of singularities using a log-log regression analysis along the crack front. The analyses showed that finite-sized cracked bodies have two singular stress fields. The near-field singular stress has the form $\sigma = C_o(\theta,z)\ r^{-1/2} + D_o(\theta,\phi)\ R^{\lambda\sigma}$. The first term is the cylindrical singularity with the power -1/2 and is dominant over the middle 96% (for Poisson's ratio = 0.3) of the crack front and becomes nearly zero at the free surface. The second singularity is a vertex singularity with the vertex point located at the intersection of the crack front and the free surface. The second singularity is dominant at the free surface and becomes nearly zero away from the boundary layer. The thickness of the boundary layer depends on Poisson's ratio of the material and is independent of the specimen type. The thickness of the boundary layer was about 0%, 2%, 4%, and 5% of the total specimen thickness for Poisson's ratio of 0.0, 0.3, 0.4, and 0.45, respectively.

Because there are two singular stress fields near the free surface, the strain-energy-release rate (G) is an appropriate parameter to measure the severity of the crack front. The G-distribution for M-T and bend specimens were different.

INTRODUCTION

A crack front intersecting the free surface in a three-dimensional (3D) body has been a subject of interest for the last two decades [1-12]. Hartranft and Sih [2] and Sih [3] considered a through-the-thickness crack intersecting normal to the free surfaces in a finite size plate. They argued that the classical two-dimensional (2D) singular (square root) stress and displacement fields are not valid at the free surface because such a field would yield a zero stress intensity factor and violate the physical deformation characteristics of the body, namely the nonzero deformation at the free surface. They defined a boundary-layer region (a region where the stress field is different from classical square-root singularity) of thickness β near the free surface by an empirical equation $\beta = t/(4 + 16t/a)$, in which the square-root singularity is not valid. In this equation, t is the thickness of the plate and $2a$ is the crack length. In 1977, Benthem [4,5] showed that if separation of variables is valid at the intersection of the crack front and the free surface then a vertex singularity exists. The power of the singularity is weaker than the classical value of -0.5. He analyzed a problem of a quarter-plane crack in a semi-infinite half-space subjected to symmetric loading. He expressed the near-field stresses by a vertex singularity as $\sigma = E(\theta,\phi)R^{\lambda\sigma}$ and the displacement as $v = F(\theta,\phi)R^{\lambda v}$. Both stress and displacement are in spherical coordinates, R, θ, and ϕ, with the intersection of the crack plane and the free surface as the origin. Benthem showed that the value of λ_σ varies between -0.5 and -0.332 for Poisson's ratios between 0.0 and 0.5, respectively. About the same time, Bazant and Estenssoro [6,7] presented identical results using a 3D finite-element analysis.

Later efforts, both analytical [8] and experimental [9], focused on confirming results obtained by Benthem [4,5] and Bazant and Estenssoro [6,7]. Smith and his co-workers [9-11] used stress freezing photoelastic experiments to measure the power of the singularity along the crack front. They assumed that the near-field stresses and displacements are represented by an extended classical 2D singularity equation. (In this paper such a singularity is referred to as a cylindrical singularity.) By invoking the separation of variables assumption, they calculated the stress singularity from the power of the displacement field equation $v = B_o r^{\lambda_v}$. Their predicted free-surface singularity for a Poisson's ratio ν of 0.40 agreed reasonably well with Benthem's results. Furthermore, the measured power of the singularity changed monotonically from -0.5 at the interior to -0.37 at the free surface. The transition region near the free surface was about 20% of the specimen thickness.

One common assumption in all the above studies is that the space variables are separable in the near-field stress and displacement equations. The validity of this assumption itself is not known. Furthermore, the variation of λ_σ and λ_v within the boundary-layer region has not been analytically investigated for finite-size cracked bodies. Recently, Shivakumar and Raju [12], through a superposition analysis, showed that for a middle cracked tension (M-T) specimen, the near-field stress has two singularities. The form of the near-field stress is given by $C_o\, r^{-1/2} + D_o\, R^{\lambda_\sigma}$, where the first term is the classical square-root singularity and the second term is probably Benthem's vertex singularity. The objectives of the present paper are to extend the work reported in reference 12 to various specimen configurations, to use different Poisson's

ratios, to evaluate the thickness of the boundary layer region, and, finally, to evaluate the strain-energy-release rate at the intersection of the crack front and the free surface. In the literature [6-8], the drop in the strain-energy-release rate or stress-intensity factor the near-free surface region has been attributed to the deviation of near-field stress from the classical square-root singularity. The validity of this hypothesis will also be evaluated.

Middle-crack tension (M-T) and bend specimens, shown in Figure 1, with homogeneous, isotropic, and elastic properties were considered. Finite-element analyses using 20-node isoparametric elements were performed. The M-T specimen was analyzed with several values of Poisson's ratios and two values of thicknesses. In each case, the displacement and stress fields around the crack front were evaluated. The power of the singularity of the mode I stress field was evaluated from the finite-element results using the log-log least square procedure in reference 12. The power of the singularity at the free surface is compared with Benthem [4,5] results for a quarter plane crack in a semi-infinite solid. The effect of Poisson's ratio on the distribution of the power of the singularity in the boundary layer region is assessed. In this paper, some of the analysis and results presented in reference 12 are repeated for the purpose of completeness and clarity.

Because the stress-intensity factor (K) is based on an assumed square-root singularity, it may not be a valid parameter to measure the severity of a crack front in the boundary-layer region where the power of the singularity is unknown. On the other hand, the strain-energy-release rate (G), which requires no such assumption, is an appropriate alternate fracture

parameter. Therefore, the strain-energy-release rate is used to characterize the severity of the crack front. While several methods exist to compute G, a simple and an accurate method based on the virtual crack closure technique (VCCT) developed by Shivakumar et al. [13] is used. The G-distribution for M-T and bend specimens were compared with each other. The boundary layer region, defined by the non-square-root stress singularity, is compared with the region over which G has a gradient for different specimen configurations.

NOMENCLATURE

a	crack length, m
E	Young's modulus, GPa
G	strain-energy-release rate, J/m^2
$G_{p\epsilon}$	plane-strain, strain-energy-release rate, J/m^2
H	half-height of specimen, m
P	load per unit length, N/mm
R, θ, ϕ	spherical coordinate system
r, θ, z	cylindrical coordinate system
S	remote tension stress, N/mm^2
t	specimen thickness, m
t_i	ith layer thickness, m
u,v,w	displacements in x-, y-, and z-directions, m
x,y,z	Cartesian coordinates, m
W	half-width of the specimen, m
λ_σ	power of the stress singularity
λ_v	power of displacement field

ν Poisson's ratio

σ_y normal stress in y-direction, GPa

TREATMENT OF SINGULARITIES IN CRACKED BODIES

In this section, the mathematical forms of 2D and 3D singular stress fields and the corresponding displacement fields near a crack front are discussed.

Two-Dimensional Problems

The classical solution to the 2D crack problems was given by Westergaard [17] and Williams [18]. The near-field stress singularity was found to be of the square-root-r type, where r is the radius vector measured from the crack tip. The near-field stresses and displacements can be expressed in a variable separable form, in terms of polar coordinates r and θ, as

$$\sigma = A(\theta)\, r^{\lambda_\sigma}$$

and

$$v = B(\theta)\, r^{\lambda_v}$$

with $\lambda_\sigma = -0.5$ and $\lambda_v = 0.5$. The terms A and B are functions of θ only. This type of stress singularity is referred to as a polar singularity.

Three-Dimensional Problems

For 3D crack problems, two forms of singularities have been postulated: the cylindrical singularity, which is an extension of the 2D polar

singularity to 3D problems, and the vertex singularity, which is assumed to exist at the intersection of the crack front and the free surface [4-7]. This section discusses these two singularities.

Cylindrical singularity.- This is a direct extension of the 2D polar singularity of near-field stresses along the crack front. Figure 2 shows the cylindrical coordinate system r, θ, z with the crack front along the z-axis. The near-field stresses and displacements at a point P are assumed to be

$$\sigma = A_o(\theta,z)\ r^{\lambda\sigma} \tag{1}$$

and

$$v = B_o(\theta,z)\ r^{\lambda v} \tag{2}$$

where λ_σ is the power of stress singularity and λ_v is the power of displacement field. A_o and B_o are functions of only θ and z. Because a cylindrical coordinate system with the crack front as the z-axis is used in Eqs. 1 and 2, this singularity is termed as a *cylindrical singularity*. If λ_σ and λ_v are independent of θ for all values of z and $\lambda_\sigma = \lambda_v - 1$, then Eqs. 1 and 2 are valid for the complete crack front. Eqs. 1 and 2 reduce to classical square-root singularity if $\lambda_\sigma = -0.5$ and $\lambda_v = 0.5$. However, these equations cannot be valid at the free surface $z = t/2$ [3].

Vertex singularity.- As previously explained, Benthem postulated the vertex singularity at the intersection of the crack front and the free surface, point Q in Figure 2, in the form of

$$\sigma = E(\theta,\phi)\ R^{\lambda\sigma} \tag{3}$$

and

$$v = F(\theta,\phi)\ R^{\lambda v} \tag{4}$$

where R is the distance between the vertex point Q and the point P.

The terms E and F are independent of R and functions of θ and ϕ only. The exponents λ_σ and λ_v are constants and are functions of only Poisson's ratio. Furthermore, Eqs. 3 and 4 assume that the separation of variables is valid; hence, $\lambda_\sigma = \lambda_v - 1$.

Both the cylindrical and vertex forms of the singularities are based on the fundamental assumption that the separation of space variables is applicable to the stress and displacement fields near the crack front. However, the validity of this assumption has not been proven. In the next section, a new look at the 3D problem based on superposition is used to hypothesize the singular stress fields.

Superposition Analysis

The complete stress and displacement fields in a linear elastic cracked body, for example, the M-T specimen, can be hypothesized to be the sum of two solutions: a plane-strain solution and a 3D solution where surface tractions are prescribed on the $z = \pm t/2$ planes, as shown in Figure 3. The plane-strain solution requires the displacements w to be zero on the $z = \pm t/2$ planes. This constraint produces tractions σ_z on these planes. Therefore, the negative of these surface tractions need to be imposed on the second problem (Fig. 3c) to satisfy the stress-free conditions on the $z = \pm t/2$ planes in the original 3D problem. For convenience of presentation, the second problem is referred to as the residual problem. This superposition analysis is schematically shown in Figure 3. Thus, the near-field stress for the original 3D problem can be expressed as

$$\sigma = C_o'(\theta)\, r^{-1/2} + T'(r,\theta,z) \qquad (5)$$

The first term is the solution to the plane-strain problem, with the

classical square-root-r singularity and the coefficient C_o is function of only θ and not of z. The second term is a solution to the residual problem, which could also have a singular field with a power different from -0.5 [3]. Therefore, a 3D cracked body, in general, can have two singular stress fields. Since the residual problem is also a 3D problem, its solution can also have two singular stress fields: a square-root singularity and an unknown singular field. Therefore, $T'(r,\theta,z)$ is expressed as

$$T'(r,\theta,z) = C_o''(\theta,z)\ r^{-1/2} + T(r,\theta,z) \qquad (6)$$

Combining Eqs. 5 and 6, the general solution to the near-field stresses for the original 3D cracked body is

$$\sigma = C_o(\theta,z)\ r^{-1/2} + T(r,\theta,z) \qquad (7)$$

The first term in the Eq. 5 is the square-root singular field and the second term is the general singularity, which needs to be established. The term C_o, which is a function of the polar angle θ and the distance from the mid-plane z, defines the magnitude of the square-root singular stress field. For very thick specimens the interior develops a plane strain stress state and, hence, in the interior only the square-root singular stress field exists. Several investigators, including the present analysis, [14-16] have found in 3D analyses of cracked bodies that plane-strain constraints exist for most of the crack front. Therefore, $T(r,\theta,z)$ must become zero in the interior and non-zero away from the mid-plane region.

The second term $T(r,\theta,z)$ can be expressed either as a cylindrical or vertex singularity using cylindrical or spherical coordinate system, respectively. Hence, Eq. 7 is rewritten as

$$\sigma = C_o(\theta,z)\ r^{-1/2} + D_o(\theta,z)\ r^{\lambda\sigma} \qquad (8)$$

or

$$\sigma = C_o(\theta,z)\ r^{-1/2} + E_o(\theta,\phi)\ R^{\lambda_\sigma} \qquad (9)$$

Here λ_σ is the unknown power of singularity and the term D_o is a function of θ and z and E_o is function of θ and ϕ. At the free surface ($z = \pm t/2$), $R = r$; hence Eq. 9 reduces to Eq. 8. Eqs. 8 and 9 assume that a variable separable form is valid. If this assumption is not valid, then the finite element results would show a dependency on θ. At $z = t/2$, the value of λ_σ must be other than -0.5 to satisfy the compatibility requirement suggested by Sih [3]. It is clear from Eqs. 8 and 9 that the plane strain solution is a special case of the 3D solution wherein the coefficient D_o (or E_o) is zero and C_o is constant for all values of z.

The displacement field for the cracked body can be expressed, similarly, in a two-term form as

$$v = F_o(\theta,z)\ r^{1/2} + G_o(\theta,z)\ r^{\lambda_v} \qquad (10)$$

or

$$v = F_o(\theta,z)\ r^{1/2} + H_o(\theta,\phi)\ R^{\lambda_v} \qquad (11)$$

The terms F_o and G_o are functions of θ and z; and H_o is a function of θ and ϕ. The exponent λ_v is the power of the displacement field. As already explained, in the interior of the crack front, C_o and F_o are dominant and the other coefficients are either zero or have negligible influence. But in the neighborhood of the free surface ($z = t/2$), the coefficients of the second singularity become dominant. Because strains (and, hence, stresses) are the first order derivatives of the displacements, for the displacements in Eqs. 10 and 11 to represent the stress field in Eqs. 8 and 9, λ_σ should be equal to $\lambda_v - 1$. If λ_σ is not equal to

λ_v - 1, then the variable separable form is not valid in Eqs. 8-11. Further, if Eqs. 8 and 9 are the correct form for stresses then Eqs. 10 and 11 are not correct for displacements and vice versa.

Evaluation of Second Singular Stress Field

Using stresses and displacements from an accurate numerical solution (such as a finite-element analysis), the coefficients in Eqs. 8-11 can, in principle, be evaluated. The coefficients C_o, D_o, E_o, and the exponent λ_σ from the stress data and F_o, G_o, H_o and λ_v from the displacement data are to be evaluated along the crack front. The problem reduces to the evaluation of two constants and an exponent (λ_σ or λ_v) for each of the Eqs. 8-11. Several numerical procedures were attempted but none proved reliable to evaluate two unknown coefficients and an unknown exponent in Eqs. 8-11. However, reliable numerical procedures are available to evaluate one constant and one exponent. Therefore, Eqs. 8-11 were examined to reduce the problem to one coefficient and one unknown exponent. Thus, the stress and displacement are represented by

$$\sigma = C_b \, r^{\lambda_\sigma} \tag{12}$$

and

$$v = G_b \, r^{\lambda_v} \tag{13}$$

For the purpose of discussion, the crack front is considered to be divided into three regions: the interior region, the boundary-layer region, and the free surface location (region). The interior region is the region where the stress field is dominated by the square-root singularity (the first term in Eqs. 8-11). The boundary-layer region is the region near the free surface and beyond the square-root singularity dominant region. The

free surface ($z = 0.5t$) is a special location in the boundary-layer region. Here, Eq. 9 reduces to Eq. 8 and Eq. 11 reduces to Eq. 10 because $R = r$. As mentioned previously, in the interior region, the contribution of the second singularity to total stresses and displacements is nearly zero. In this region Eqs. 12 and 13 are valid approximations and, therefore, a fit to the finite-element results should give $\lambda_\sigma = -0.5$, $\lambda_v = 0.5$, and establish the square-root singular region. Because the stresses and displacements in the interior are already known to be square-root singular, only the singularity field in the boundary-layer region needs to be analyzed. The coefficients in Eqs. 8 and 9 have the following three possible conditions in the boundary-layer region and at the free surface:

a. $C_o(\theta,z)$ is dominant and constant all along the crack front. That is, $C_o(\theta,z) = C_o(\theta,0)$ for $0 \le z \le t/2$.

b. $C_o(\theta,z)$ is dominant in the interior of the crack front, varies along the z-axis, and, at the free surface ($z = t/2$), C_o is zero or very small compared to the second term in Eqs. 8 and 9.

c. $C_o r^{-1/2}$ is of the same order of magnitude as $D_o r^{\lambda_\sigma}$ or $E_o R^{\lambda}$.

If the condition (a) is true, then the constants C_o and F_o can be evaluated using stress data at the midplane ($z = 0$). Eqs. 8 and 9 can now be rewritten as

$$\sigma - C_o(\theta,0)\, r^{-1/2} = D_o\, r^{\lambda_\sigma}$$

and

$$\sigma - C_o(\theta,0)\, r^{-1/2} = E_o\, R^{\lambda_\sigma} \qquad (14)$$

Similarly, for displacements

$$v - F_o(\theta,z)\, r^{1/2} = G_o\, r^{\lambda_v}$$

and

$$v - F_o(\theta,z)\, r^{1/2} = H_o\, R^{\lambda_v} \tag{15}$$

The left-hand-side values of Eqs. 14 and 15 are known for various values of r and hence a fit can be made to determine the constants D_o, E_o, G_o, and H_o and the exponents λ_σ and λ_v. If the computed λ_σ and λ_v are same for various angles θ and satisfy the condition $\lambda_\sigma = \lambda_v - 1$, then the variable separable form is valid. Otherwise, either the condition (a) or the variable separable form for the second singularity is not valid.

If the condition (b) is true, then, at the free surface ($z = t/2$), Eqs. 8 and 10 reduce to Eqs. 12 and 13, respectively, as

$$\sigma = D_o\, r^{\lambda_\sigma} \tag{16}$$

and

$$v = G_o\, r^{\lambda_v} \tag{17}$$

The exponents λ_σ and λ_v can easily be calculated from finite-element stresses and displacements using Eqs. 16 and 17, respectively. If λ_σ and λ_v show independence with θ, and $\lambda_\sigma = \lambda_v - 1$, then the variable separable form and condition (b) are valid. Otherwise, either condition (b) or the variable separable form is not valid. Within the boundary-layer region, Eqs. 16 and 17 are not correct representations of stresses (Eqs. 8-9) and displacements (Eqs. 10-11) because both terms are dominant. Therefore, even if λ_σ and λ_v are independent of θ at $z = t/2$, they will show dependence on θ at $z < t/2$. If such a condition exists, then the condition (b) is still valid.

If the condition (c) is true, the stresses and displacements cannot be represented in a one-term form as in Eqs. 12-13. Therefore, a numerical

fit to Eqs. 12-13 will yield meaningless values for λ_σ and λ_v. Also, even if the variable separable form for stresses and displacements is valid, λ_σ and λ_v would show dependence on θ.

In summary, two fits in the form of Eqs. 14-17 are needed to determine the form of the singular stress in the boundary-layer region and free-surface location. If a fit to Eqs. 14 and 15 produces λ_σ and λ_v values independent of θ and $\lambda_\sigma = \lambda_v - 1$, then condition (a) is valid and the second singularity is given by λ_σ. If a fit to Eqs. 16-17 produces λ_σ and λ_v values independent of θ, satisfies the condition $\lambda_\sigma = \lambda_v - 1$ at $z = t/2$, and is dependent on θ within the boundary-layer region ($z < t/2$), then condition (b) is valid and the second singularity is given by λ_σ of Eq. 16. If λ_σ and λ_v are dependent on θ at $z = t/2$ and in the boundary-layer region, then condition (c) is valid. Then λ_σ and λ_v can only be determined by a fit to two coefficients and one exponent.

FINITE-ELEMENT ANALYSIS

Specimen Configuration

Figure 1 shows a middle-crack tension (M-T) specimen with uniform applied stress S and a bend specimen with a line loading P. All results presented, unless otherwise stated, refer to $S = 1$ N/mm^2 or $P = 1$ N/mm. The values of the geometric parameters defined in the Figure 1 are $W = 50$ mm, $H = 200$ mm, and $a = 25$ mm. Two specimen thicknesses (t), 25 mm and 50 mm, were considered for the M-T specimen and one thickness 25 mm was used for the bend specimen. The material was assumed to be homogeneous and isotropic with an elastic modulus $E = 70$ GPa and a Poisson's ratio $\nu = 0.3$. For the M-T specimen with $a/t = 1$ several values with ν ranging

from 0.0 to 0.45 were used. Exploiting the symmetry in the specimen geometry and loading, only one-eighth of the M-T specimen and one-fourth of the bend specimen was modeled in the finite-element analysis.

Finite-Element Model

Figure 4 shows the finite-element idealization of one-eighth of the M-T or one-fourth of the bend specimen. Twenty-node isoparametric elements were used every where except along the crack front, where pentahedron elements (15 nodes) were used. The insert in the figure describes idealization near the crack front in the x-y plane. In pentahedron (collapsed) elements, the intermediate nodes were retained at the mid-sides of the element edges. Note that a square-root singularity of the stress and displacement fields would have been reproduced if the mid-side nodes were moved to the quarter points [19-21]. This was not done since it would have biased the stress field singularity at the crack front. Instead, the singularity was calculated from the computed stresses ahead of the crack front.

The 3D finite-element model was developed using a 2D idealization of the $z = 0$ plane and then translating that plane in the z-direction. Adequacy of the inplane (x-y) and through-the-thickness (z-direction) modeling was established by a 2D plane-strain analysis and a convergence study of the 3D models. Details of the convergence study are presented in reference 12. The model selected for the present study had nine layers of unequal thickness with 5,348 nodes; 1,116 elements; and 16,044 degrees of freedom. The layer thickness near the free surface was 0.005 mm and the smallest element size in the x-y plane was also 0.005 mm (see insert in Fig. 4). The mesh refinement increased equally in x-, y-, and z-directions

towards the vertex point Q. A local least-square smoothing procedure [20] was used to extrapolate the Gauss point stresses to the element nodes.

RESULTS AND DISCUSSION

In this section, a plane-strain analysis of the M-T specimen was performed to reproduce some of the established results in 2D crack problems. The nodal displacements and stresses near the crack front were used to evaluate power of singularity through a log-log least square regression analysis. Details of the regression analysis are presented in reference 12. Second, 3D stress and displacement fields near the crack front for the M-T specimen are presented. The power of singularities along the crack front of M-T and bend specimens are then evaluated. Finally, the effect of Poisson's ratio on the power of the singularity distribution and the specimen configuration on the G distribution are assessed.

Two-Dimensional Plane-Strain Analysis

The plane-strain analysis will verify that the finite element model can reproduce the classical 2D singular stress and displacement fields near the crack tip. The plane-strain results were obtained from the same 3D, FE model shown in the Figure 4 by specifying $w = 0$ on $z = t/2$ plane. The mode I stress σ_y and the opening displacement v were used to calculate the exponents in the stress and displacement equations. The power of singularity λ_σ was calculated by fitting a straight line to log r versus log σ_y results. The procedure was repeated along radial lines at intervals of 22.5^o for $0^o \leq \theta \leq 135^o$. A similar straight-line-fit procedure was also used for the v displacement to evaluate the exponent

λ_v. The procedure was repeated along each of the radial lines $22.5^o \leq \theta \leq 180^o$ in intervals of 22.5^o. As shown in figure 5, consistent values of λ_σ of about -0.497 were obtained for $0^o \leq \theta \leq 67.5^o$. The λ_v from this fit was 0.505 at $\theta = 180^o$ and varied less than 1% for θ between 112.5^o and 180^o.

The fit to the σ_y stresses for $\theta \geq 90^o$ gave λ_σ values that deviated by more than 2% from the classical value of -0.5. Similarly, for $\theta \leq 90^o$, the fit to the v-displacements gave λ_v values that deviated by more than 2% from 0.5. The variations in the λ_σ values for $\theta \geq 90^o$ (λ_v values for $\theta \leq 90^o$) is expected. Since the magnitude of σ_y and v decreases and eventually approaches zero at $\theta = 180^o$ and $\theta = 0^o$, respectively. Hence, the log-log fit is expected to yield accurate results only in the regions where σ_y and v are non-zero. For this reason, these values are not shown in Figure 6.

Figure 5 shows that the exponents λ_σ and λ_v are independent of the polar angle θ and that they satisfy the condition $\lambda_\sigma = \lambda_v - 1$. Thus, the plane-strain finite element model accurately reproduced the variable separable form of the 2D singular field solution at the crack tip.

The 2D analysis suggests that if the exponents λ_σ and λ_v are invariant with respect to θ, then the log-log fits would yield nearly identical slopes. Therefore, the invariance of λ_σ and λ_v with respect to θ will be evaluated by comparing the values at $\theta = 0°$ and 45^o for λ_σ and at $\theta = 180^o$ and 135^o for λ_v. If the exponents are nearly identical then the invariance with respect to θ is assumed to exist. The invariance suggests that a variable separable form for stresses and displacement fields is valid in polar coordinates.

Stress and Displacement Distributions in the M-T Specimen

Figure 6 shows the distribution of stress σ_y ahead of the crack front at various z = constant planes. Note the log-log scale in the figure. The stress is normalized by the remote stress S at $y = \pm H/2$. The figure shows that both the slope and magnitude of σ_y are nearly identical for $0 \leq z/t \leq 0.4$ (results between $z/t = 0.4$ and 0.4832 were clustered together, hence, these results are not shown in the figure). For $z/t > 0.4$, the slope appeared to change and the magnitude of the stress shows a drop compared to the interior ($z/t = 0$) values. At the free boundary $z = t/2$, the slope is smaller than at the mid-plane ($z = 0$). The variation of the slope (power of singularity λ_σ) in z-direction will be discussed later.

Figure 7 shows the distribution of opening displacement v behind the crack front at various z = constant planes. Note that $S = 57$ N/mm^2 for the displacement plot. The slope of displacement curves increased towards the free surface. Furthermore, the opening displacement decreased as the free surface is approached [14-16]. The variation of the slope (exponent λ_v) in z-direction will be discussed later.

Comparison of v-displacement at $z = 0$ and $z = t/2$ at the centerplane ($x = -25$ mm) of the specimen showed that the free surface ($z = t/2$) displacement is about 4% higher than the mid plane ($z = 0$) displacement. This trend is contrary to the distribution near the crack front. However, for the bend specimen, the v-displacement was nearly constant (less than 0.2%) at $x = -25$ mm. (These results are not shown in the figure.)

Singular Stress Fields in the M-T Specimen

As previously mentioned, two types of singular stress fields (Eqs. 8 and 9) and displacement fields (Eqs. 10 and 11) are possible for a 3D cracked body. Furthermore, three regions along the crack front (interior, boundary layer, and free surface) and three possible solutions to the near-field singular stresses were identified. Here, the possibility of conditions (a) and (b) are assessed. If neither (a) nor (b) is possible then the condition (c) defines the near-field singular stresses in a 3D cracked body.

Condition (a).- In this condition, the coefficient C_o of the square-root singularity in Eqs. 8 and 9 is constant all along the crack front. If this is true, then a fit of Eqs. 14 and 15 to the finite-element stresses and displacements at $z = t/2$ should define the second singular field. The free surface stresses and displacements were subtracted from their respective mid-plane values. The resulting stresses and displacements were used to evaluate λ_σ and λ_v using a log-log regression analysis at various θ = constant lines. Table 1 shows computed values of λ_σ (at $\theta = 0^o$ and 45^o) and λ_v (at $\theta = 135^o$ and 180^o) are dependent on θ and that λ_σ is not equal to $\lambda_v - 1$. Dependence of λ_σ and λ_v on θ shows that either this condition or the variable separable form for the residual stresses and displacements is not valid.

Condition (b).- In this definition, the coefficient of the square-root singularity is dominant in the interior of the crack front and is zero or negligibly small at the free surface. As mentioned previously, the coefficient of the second singularity is negligible or zero in the interior of the crack front and becomes dominant at the free surface. Therefore, a

simplified form of Eqs. 12-13 is a valid representation for all z, except in the boundary-layer region. This type of fit should also define the region of dominance of each of the terms in Eqs. 8-11. First, to verify the validity of separation of variables, a log-log least square regression was performed at the midplane (z = 0) and at the free surface (z=t/2) for $\theta = 0^o$ and 45^o for stress σ_y and for $\theta = 135^o$ and 180^o for v-displacement. Table 2 presents λ_σ and λ_v at the mid-plane and at the free surface. At the z = 0 plane, the power of the singularity λ_σ is nearly identical to the 2D classical value of -0.5 and is same for $\theta = 0^o$ and 45^o. The corresponding slope of the v-displacement λ_v is 0.5 and is also independent of θ. These results satisfy the relationship $\lambda_\sigma = \lambda_v - 1$ both at the midplane and the free surface. Therefore, separation of variables is valid both at the midplane and at the free surface of the specimen. At the free surface, the power of the singularity is weaker ($\lambda_\sigma = -0.451$) than the square-root singularity and agrees very well with Benthem's solution [4,5]. Actually, Benthem assumed separation of variables and proved that the vertex singularity exists at the vertex point Q. Therefore, proving the validity of variable separable form for stress and displacements shows the possible existence of a vertex singularity at the free surface. However, at the free surface, R = r, a vertex singularity reduces to a cylindrical singularity. Therefore, one would argue that the second singularity could be a cylindrical singularity.

Table 3 compares λ_σ calculated at $\theta = 0^o$ and $\lambda_v - 1$ calculated at $\theta = 180^o$ with Benthem's solutions [4,5] for various Poisson's ratios ($\nu = 0.0$ to 0.45). The present values of λ_σ and $\lambda_v - 1$ agreed very well with Benthem's vertex singularity results. Therefore, the second

singularity may be a vertex singularity and the coefficients of the square-root singular term (the first term in Eqs. 8-11) at the free surface is negligibly small or identically equal to zero compared to the second term.

Figure 8 shows the variation of λ_σ and λ_v along the crack front. Both λ_σ and λ_v were evaluated by fitting Eqs. 12 and 13 to the finite-element stresses and displacements, respectively. In this figure only the results for $z/t > 0.45$ are shown. In the region $0 \leq z/t \leq 0.48$, both λ_σ and λ_v are constant and equal to the classical 2D values ($\lambda_\sigma = -0.5$ and $\lambda_v = 0.5$). This indicates that over the interior (96% of the crack front), the power of singularity is -0.5 and the influence of the second singularity is negligibly small or zero. Furthermore, at $z/t = 0.4832$ λ_σ calculated at $\theta = 0^o$ and 45^o and λ_v at $\theta = 135^o$ and 180^o did not show any significant dependency on θ. Both λ_σ and λ_v start deviating from the 2D values at $z/t > 0.48$ and become dependent on θ (except at $z = t/2$). This indicates that both singular fields in Eqs. 8-11 are becoming equally dominant and, hence, the one-term fit based on Eqs. 12 and 13 is not valid in this region. Therefore, the question of the type of the second singularity (vertex or cylindrical) is still not completely resolved unless a reliable procedure to determine two constants and an exponent is available.

In summary, a 3D cracked body has two singularities: a square-root cylindrical singularity and a vertex or cylindrical singularity. A comparison of the present results with Benthem [4,5] and Bazant and Estenssoro [6,7] results appears to show that the second singularity is a vertex singularity. The square-root singularity dominates in the middle 96% of the crack front and its coefficient is nearly zero at the free surface.

The influence of the second singularity becomes dominant near the free-surface region ($0.48 \leq z/t \leq 0.5$).

Effect of Poisson's Ratio on Boundary-Layer Thickness

Figure 9 shows the distribution of λ_σ calculated by fitting Eq. 12 to the finite-element results for Poisson's ratios of 0.0, 0.3, 0.4, and 0.45. For Poisson ratio equal to 0.0, the constitutive equations decouple and the 3D problem reduces to that of a plane-stress case with the result that λ_σ remains constant and equal to -0.5 for all z. Therefore the boundary-layer length is zero. For Poisson's ratio greater than 0.0, the boundary-layer length increased with increased values of ν. If one defines the boundary-layer length as the length over which λ_σ differed by more than 2% from the 2D classical value of -0.5, then the boundary-layer lengths are 2%, 4%, and 5% of specimen thickness for $\nu = 0.3$, 0.4, and 0.45, respectively.

Effect of Specimen Configuration on Boundary Layer

Figure 10 shows the λ_σ distribution for two M-T specimen thicknesses ($t = a$ and $t = 2a$, where $a = 25$ mm) and for a bend specimen ($t = a$) for Poisson's ratio of 0.3. The figure shows nearly identical λ_σ-distributions for all three specimens. At the free surface ($z/t = 0.5$), λ_σ for the M-T specimens with $a/t = 1.0$ and 0.5 are, respectively, -0.451 and -0.455 and, for the bend specimen, is -0.461 (which is about 2% lower than for M-T specimens). Furthermore, the boundary layer length for all three specimens is nearly same ($0.48 \leq z/t \leq 0.5$). Therefore, the specimen configuration and the loading has no effect on the λ_σ distribution and the boundary-layer length.

Strain-Energy-Release Rate Distribution for Three Specimens

This section will show that the drop in G (or K) near the free surface is not only related, as hypothesized by some investigators [6-8], to the non-square-root singularity of the stress field, but is also related to the specimen configuration and loading. Figure 11 shows the normalized G-distribution along the crack front for the two M-T specimens (a/t = 1 and 0.5) and the bend specimen. The G-distribution was calculated using the three-dimensional virtual crack closure technique of reference 13. The G-values were normalized by their respective plane-strain values ($G_{p\epsilon}$). The $G_{p\epsilon}$-values for the M-T and bend specimens are, respectively, 1.462×10^{-3} N/mm for S = 1 N/mm and 0.1148×10^{-3} N/mm for P = 1 N/mm. The normalized value of G at z = 0 (mid-plane) for the M-T specimens decreased with increasing thickness (a/t from 1.0 to 0.5). This trend indicates, as one would expect, that for smaller value of a/t, the value of G at z = 0 approaches the plane-strain value (1.462×10^{-3} N/mm). The curve of the G-distribution for the M-T specimens is nearly flat in the interior ($z/t \leq 0.4$) and shows a steep gradient near the free surface. The gradient starts at $z/t = 0.4$ for $a/t = 1.0$, and at 0.43 for $a/t = 0.5$. The curve for bend specimen shows a continuous, but small, gradient from the mid-plane (z = 0), towards the free surface. Note that, for all three specimens, the boundary layer (the region over which λ_σ deviates from the classical value of 0.5) is between $0.48 \leq z/t \leq 0.5$. Therefore, the variation of G in the region of $0 \leq z/t \leq 0.48$ cannot be attributed only to a non-square root singular stress field. Instead, the variation is also due to the specimen configuration and loading.

Strain-Energy-Release Rate at Intersection of Crack Front and Free Surface

In this section, the strain-energy-release rate at the intersection of the crack front and the free surface is evaluated using the virtual crack closure technique[13]. At the free surface ($z = t/2$), $R = r$ and Eqs. 8 and 9 reduce to Eqs. 10 and 11, respectively. For self-similar crack growth, Irwin's crack closure integral [19] is used to calculate the strain-energy-release rate. The mode I strain-energy-release rate G is written in terms of stress σ_y and displacement v as

$$G = \lim_{\Delta \to 0} 2 \left\{ \frac{1}{2\Delta} \int_0^{\Delta} \sigma_y(r,0,t/2) \cdot v(\Delta-r,0,t/2)\, dr \right\} \qquad (18)$$

Substituting σ_y and v from Eqs. 8 and 10, respectively, and using condition (b), i.e., $\lambda_v = \lambda_\sigma + 1$ one has

$$G = \lim_{\Delta \to 0} \frac{1}{\Delta} \int_0^{\Delta} \left[\left(C_o\, r^{-1/2} + D_o\, r^{\lambda_\sigma} \right) \left\{ F_o(\Delta-r)^{1/2} + G_o(\Delta-r)^{(\lambda_\sigma+1)} \right\} \right] dr \qquad (19)$$

The Eq. 19 is expanded and rewritten as

$$G = \lim_{\Delta \to 0} \frac{1}{\Delta} \int_0^{\Delta} \left[C_o F_o r^{-1/2} (\Delta-r)^{1/2} + C_o G_o\, r^{-1/2} (\Delta-r)^{(\lambda_\sigma+1)} + D_o F_o r^{\lambda_\sigma} (\Delta-r)^{1/2} + D_o G_o r^{\lambda_\sigma} (\Delta-r)^{(\lambda_\sigma+1)} \right] dr \qquad (20)$$

The integral of Eq. 20 is written as

$$G = \lim_{\Delta \to 0} \left[(\pi/2)\, C_o F_o + C_o G_o I_1 + D_o F_o I_2 + D_o G_o I_3 \right] \quad (21)$$

Where

$$I_1 = \frac{1}{\Delta} \int_0^{\Delta} r^{-1/2}\, (\Delta - r)^{(\lambda_\sigma + 1)} dr$$

$$I_2 = \frac{1}{\Delta} \int_0^{\Delta} r^{\lambda_\sigma}\, (\Delta - r)^{1/2}\, dr$$

and

$$I_3 = \frac{1}{\Delta} \int_0^{\Delta} r^{\lambda_\sigma}\, (\Delta - r)^{(\lambda_\sigma + 1)} dr$$

The integrals I_1, I_2, and I_3 are functions of Δ and λ_σ. For Poisson's ratios greater than zero, the value of λ_σ is greater than (algebraically) -0.5. Using this condition and taking the limit, the integrals I_1, I_2, and I_3 approach zero. Hence Eq. 21 reduces to

$$G = (\pi/2)\, C_o\, F_o \quad (22)$$

As previously shown, C_o and F_o are zero at the free surface. This leads to zero value for G. A zero value of strain-energy-release rate in the presence of a stress singularity appears contradictory. However, it simply means that a crack front normal to the free surface cannot grow self-similarly, as was assumed in the above discussion. Alternatively, a zero value of G at $z = t/2$ makes the crack front stationary at the vertex point Q while the crack grows in the interior. Such crack-growth behavior has been observed in many experimental studies. Crack growth in

the interior only would cause the crack front to curve and change the angle of intersection between the crack front and the free surface to more than 90^{o}, which would in turn affect the singularity field. The change in intersection angle can influence λ_{σ} and would probably increase the magnitude of C_{o} and F_{o} in Eq. 22. Thus, G would have a nonzero value at the free surface. In fact, a condition may be reached such that the G at the free surface may become equal to the interior value. The angle at which this might occur should depend on the Poisson's ratio of the material since λ_{σ} depends on Poisson's ratio (see Table 3) and the specimen type or loading.

CONCLUDING REMARKS

Three dimensional finite-element analyses of middle-crack tension (M-T) and bend specimens were performed. Twenty-node, isoparametric elements were used in the model. The displacements and stresses from the analysis were used to estimate the power of the singularities along the crack front. A log-log regression analysis was used to calculate the power of the stress singularity. The finite-element model and the regression analysis procedure were verified by analyzing a two-dimensional (2D) plane-strain problem. The calculated power of the singularity of the stress field agreed very well with the classical solution. The following conclusions were made from this study.

In finite-sized three-dimensional cracked bodies, two singularities exist along the crack front and the near-field stresses have the form $\sigma = C_{o}\ r^{-1/2} + D_{o}\ R^{\lambda\sigma}$. The first term is a cylindrical singularity with a power of -1/2, which is same as the classical 2D value. The second term may

be a vertex or cylindrical singularity. Comparison of the present results with the literature suggests the possibility that the second singularity is a vertex singularity with the power λ_σ and located at the intersection of crack front and the free surface. For a Poisson's ratio of 0.3, the cylindrical singularity dominates over 96% of the interior of the crack front while the second singularity dominates at the free surface. Within the region $0.48 \leq z/t < 0.5$, both singularities are present and the region is referred to as the boundary layer. The calculated power of the vertex singularity λ_σ at the free surface agreed very well with Benthem's results for all Poisson's ratios.

The separation of variables assumption in the stress and displacement fields was found to be valid at the free surface and in the middle 96% of the crack front for $\nu = 0.3$. Hence, this assumption may be valid in the boundary-layer region as well. The thickness of the boundary layer was found to depend on Poisson's ratio and not on the specimen configuration or loading. The boundary layer is zero for $\nu = 0.0$ and 2%, 4%, and 5% of the specimen thickness for $\nu = 0.3$, 0.4, and 0.45, respectively.

Because two singular stress fields exist within the boundary-layer region, the strain-energy-release rate G is an appropriate parameter to define the severity of the crack all along the crack front. Three specimen configurations were analyzed; the G-distribution for all three specimens showed steep gradients near the free surface. The drop in G near the free surface is not only due to the non-square root singularity but also due to the specimen configuration and loading. The region where the drop in G occurred was 10% and 7% of the crack front (measured from the free surface), for the M-T specimens of $a/t = 1.0$ and 0.5, respectively. For the bend

specimen, the G curve had a continuous gradient all along the crack front and steep gradient near the free surface. G where the crack front intersects the free surface at an angle of 90° was found to be zero. Therefore, crack growth cannot occur at the free surface if the crack front is normal to the free surface. For crack growth at the surface, the intersection angle should be greater than 90^{o} and the angle at which crack growth will occur depends on Poisson's ratio.

ACKNOWLEDGEMENTS

The authors are deeply indebted to Dr. J. H. Crews, Jr., for many inspiring discussions and for drawing attention to the superposition principle. The authors take this opportunity to thank him. This work was performed at the NASA Langley Research Center as part of NASA Contracts NAS1- 18256 and NAS1-18599.

REFERENCES

1. Sih, G. C.; Williams, M. L.; and Swedlow, J. L.: Three-Dimensional Stress Distribution Near a Sharp Crack in a Plate of Finite Thickness. AFML-TR-66-242, Air Force Materials Laboratory, Wright-Patterson Air Force Base, 1966.

2. Hartranft, R. J.; and Sih, G. C.: An Approximate Three-Dimensional Theory of Plates with Application to Crack Problems. Int. J. Engng. Science, Vol. 8, 1970, pp. 711-729.

3. Sih, G. C.: A Review of the Three-Dimensional Stress Problem for a Cracked Plate. Int. J. Fracture Mechanics, Vol. 7, No. 1, 1971, pp. 39-61.

4. Benthem, J. P.: State of Stress at the Vortex of a Quarter-Infinite Crack in a Half-Space. Int. J. Solids and Structures, Vol. 13, 1977, pp. 479-492.

5. Benthem, J. P.: The Quarter-Infinite Crack in a Half-Space: Alternate and Additional Solutions. Int. J. Solids and Structures, Vol. 16, 1980, pp. 119-130.

6. Bazant, Z. P.; and Estenssoro, L. F.: General Numerical Method for Three-Dimensional Singularities in Cracked or Notched Elastic Solids. Advances in Research on the Strength and Fracture of Materials, D. M. R. Taplin, Ed., Vol. 3a, Pergamon Press, Oxford, 1977, pp. 371-385.

7. Bazant, Z. P.; and Estenssoro, L. F.: Surface Singularity and Crack Propagation. Int. J. Solids and Structures, Vol. 15, 1979, pp. 405-426.

8. Solecki, J. S.; and Swedlow, J. L.: On the Three-Dimensional Implications of LEFM: Finite Element Analysis of Straight and Curved Through-Cracks in a Plate. Fracture Mechanics Sixteenth Symposium, M. F. Kanninen and A. T. Hopper, Eds., ASTM STP 868, American Society for Testing and Materials, Philadelphia, 1985, pp. 535-553.

9. Smith, C. W.; Epstein, J. S.; and Olaosebikan, O.: Boundary Layer Effects in Cracked Bodies: An Engineering Assessment. Fracture Mechanics: Seventeenth Volume, J. H. Underwood, R. Chait, C. W. Smith, D. P. Wilhem, W. A. Andrews, and J. C. Newman, Eds., ASTM STP 905, American Society for Testing and Materials, Philadelphia, 1986, pp. 775-788.

10. Smith, C. W.; Epstein, J. S; and Olaosebikan, O.: Advances in Aerospace Structures, Materials and Dynamics, ASME-Aero Div.-06, 1983, pp.119-126.

11. Smith. C. W. and Epstein, J. S.: Measurement of Three Dimensional Effects in Cracked Bodies, Proceedings, 5th International Congress on Experimental Stress Analysis, June 1984.

12. Shivakumar, K. N.; and Raju, I. S.: Treatment of Singularities in a Middle-Crack Tension Specimen, 21st National Symposium on Fracture Mechanics, Annapolis, MD, June 28-30, 1988.

13. Shivakumar, K. N.; Tan, P. W.; and Newman, J. C., Jr.: A Virtual Crack-Closure Technique for Calculating Stress-Intensity Factors for Cracked Three-Dimensional Bodies. Int. J. Fracture, Vol. 36, March 1988, R43-R50.

14. Raju, I. S.; Shivakumar, K. N.; and Crews, J. H., Jr.: Three-Dimensional Elastic Analysis of a Composite Double-Cantilever-Beam Specimen. AIAA Paper No. AIAA-87-0864, AIAA/ASME/ASCE/AHS 28th Structures, Structural Dynamics, and Materials Conference, Monterey, CA, April 1987.

15. Raju, I. S.; and Newman, J. C., Jr.: Three-Dimensional Finite Element Analysis of Finite-Thickness Fracture Specimens. NASA TN D-8414, 1977.

16. Atluri, S. N.; Kathiresan, K.; and Kobayashi, A. S.: Three-Dimensional Linear Elastic Fracture Mechanics Analysis by a Displacement Hybrid Finite Element Model. Paper No. L-7/3, Trans. 3rd Conf. on Structural Mechanics in Reactor Technology, London, Sept. 1975.

17. Westergaard, H. M.: Bearing Pressures and Cracks. J. Appl. Mech., Vol. 61, 1939, pp. A49-53.

18. Williams, M. L.: On the Stress Distribution at the Base of a Stationary Crack, J. Appl. Mech., Vol. 24, 1957, pp. 109-204.

19. Irwin, G. R.: Analysis of Stresses and Strains Near the End of a Crack Traversing a Plate. J. Appl. Mech., Vol. 24, 1957, pp. 361-364.

20. Hinton, E.; Scott, F. C.; and Ricketts, R. E.: Local Least Square Stress Smoothing for Parabolic Isoparametric Elements. Int. J. Num. Meth., Vol. 9, 1975, pp. 235-256.

Table 1: Variation of λ_σ and λ_v in θ-direction, at the free-surface for condition (a).

θ Deg.	λ_σ	λ_v
0	-0.534	----
45	-0.590	----
135	----	0.330
180	----	0.300

Table 2: Power of stress (λ_σ) and displacement (λ_v) fields at the mid-plane and at free surface of a M-T Specimen (ν = 0.3).

θ Deg.	Mid-plane (z = 0)		Free Surface (z = t/2)	
	λ_σ	λ_v	λ_σ	λ_v
0.0	-0.495	----	-0.451	----
45.0	-0.494	----	-0.442	----
135.0	----	0.510	----	0.556
180.0	----	0.505	----	0.548

Table 3: Comparison of present results with Benthem's solution at free surface.

Poisson's ratio, ν	Benthem[4,5] λ_σ	Present Results λ_σ	Present Results $\lambda_v - 1$
0.0	-0.500	-0.497	-0.497
0.30	-0.452	-0.451	-0.452
0.40	-0.414	-0.407	-0.417
0.45	----	-0.356	-0.391
0.50	-0.332	----	----

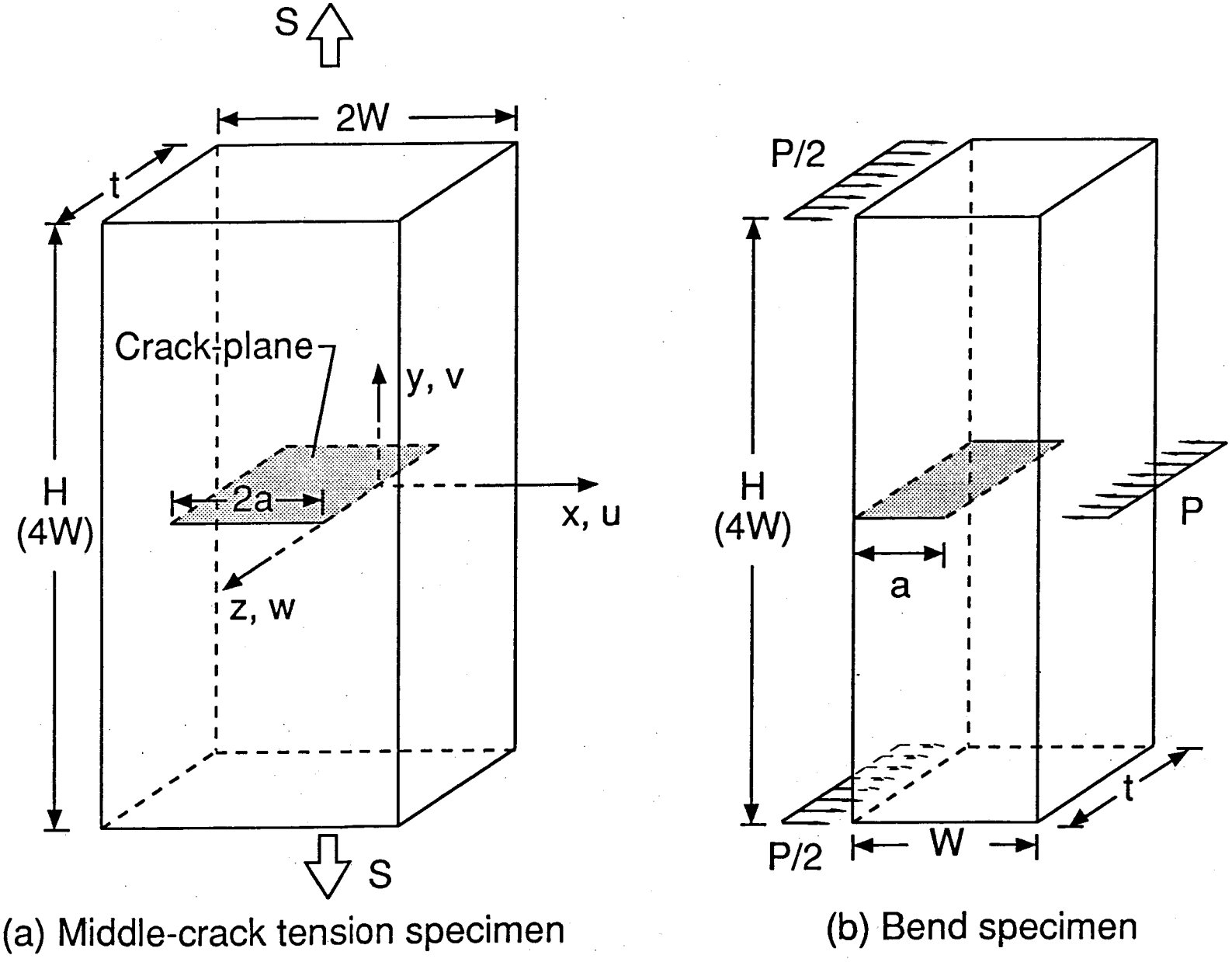

Figure 1.- Specimen configurations and loading

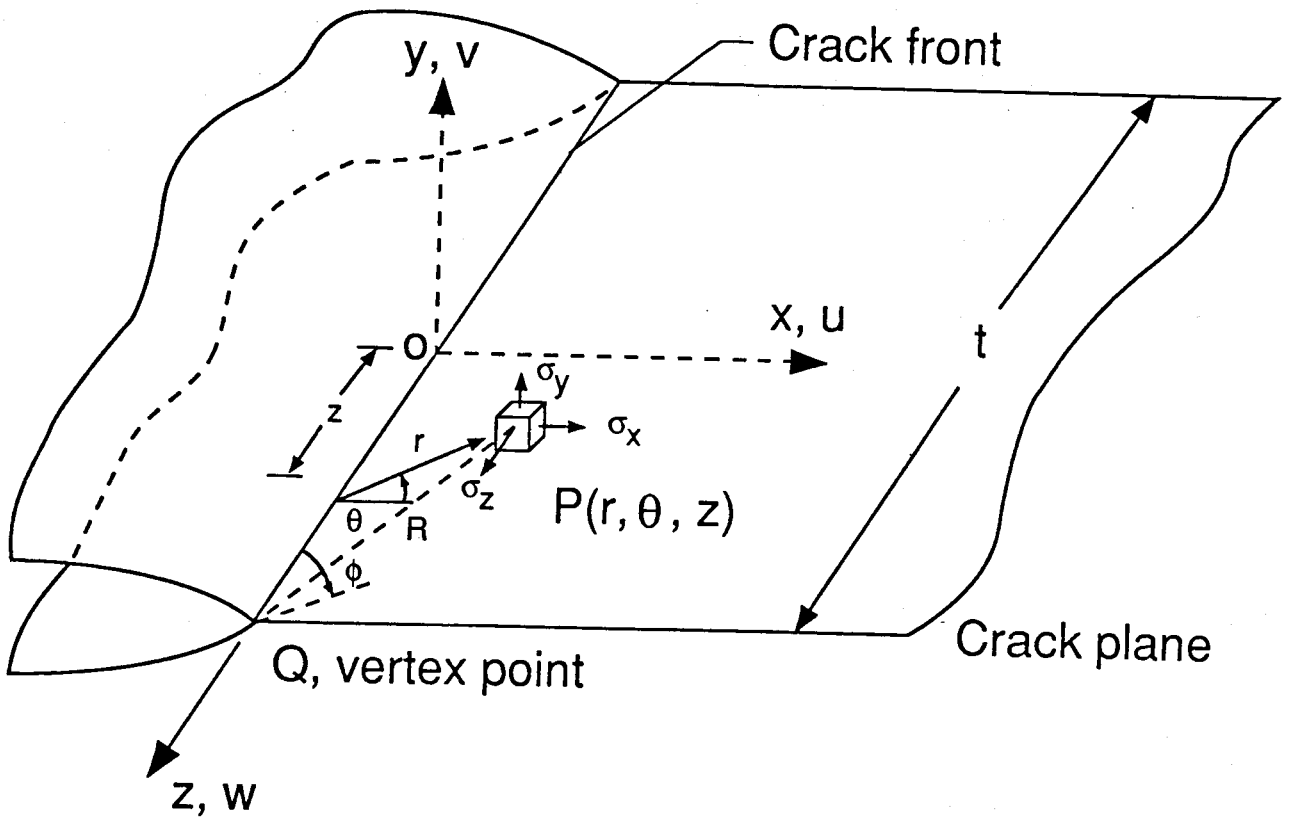

Figure 2.- Coordinate system and normal stresses at a point P

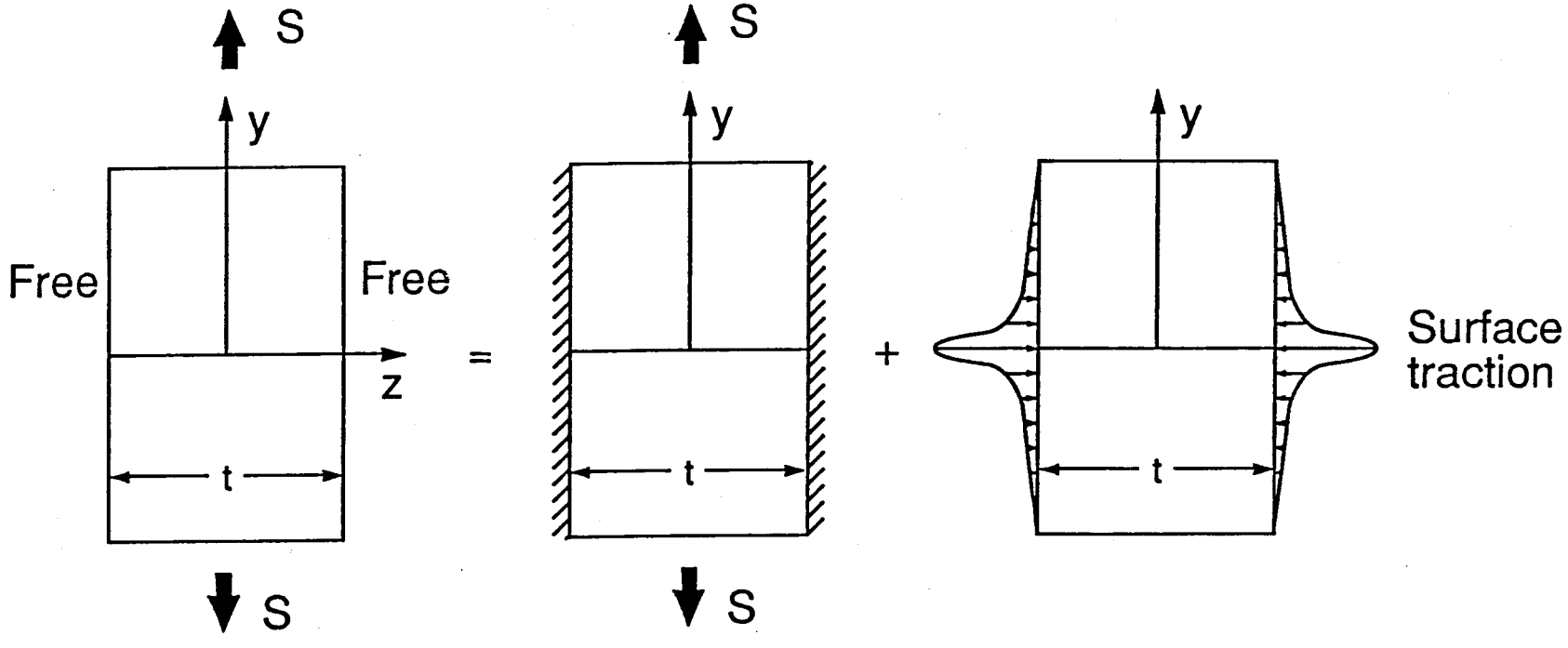

Figure 3.- Schematic of superposition analysis

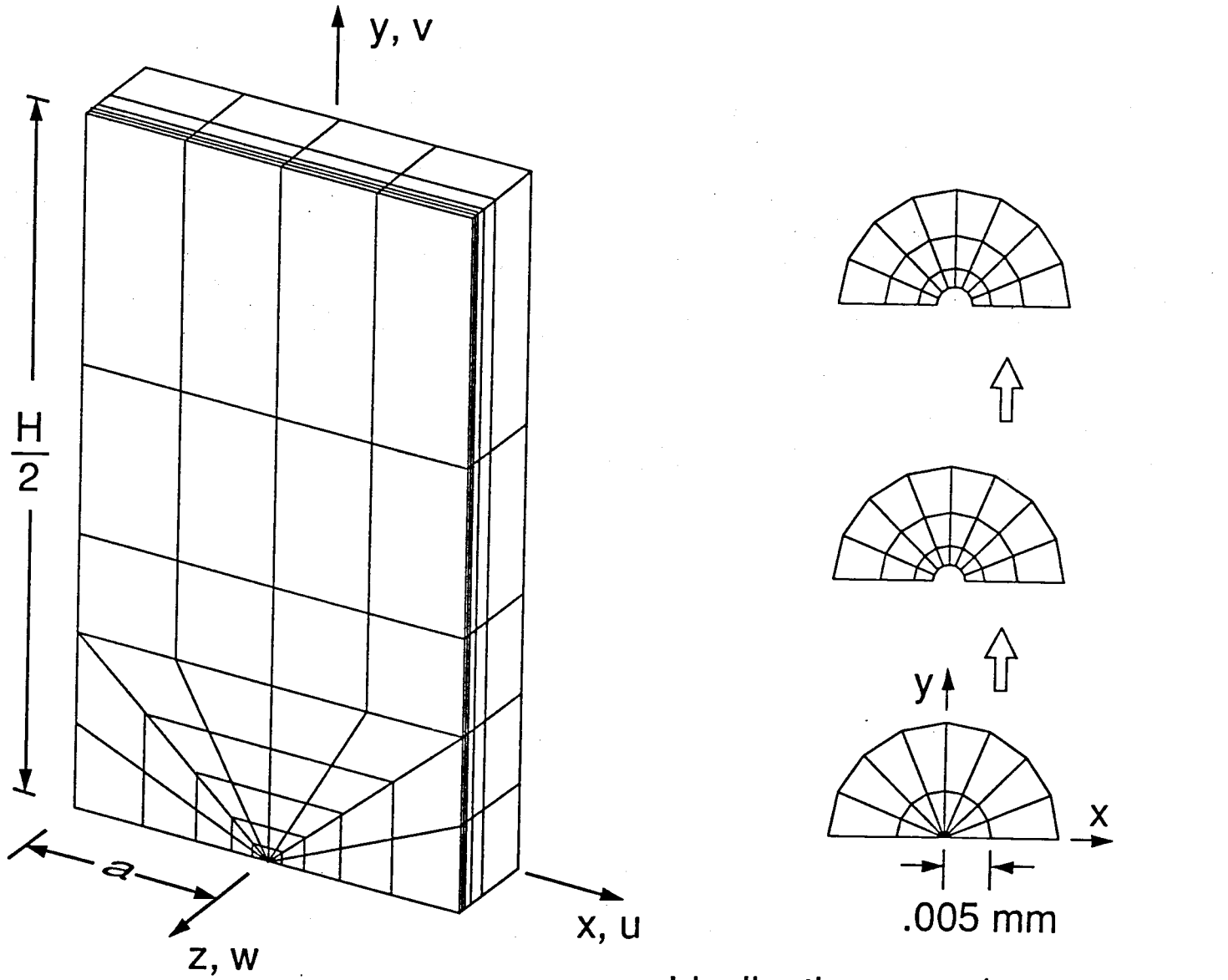

Figure 4.- Finite-element idealization

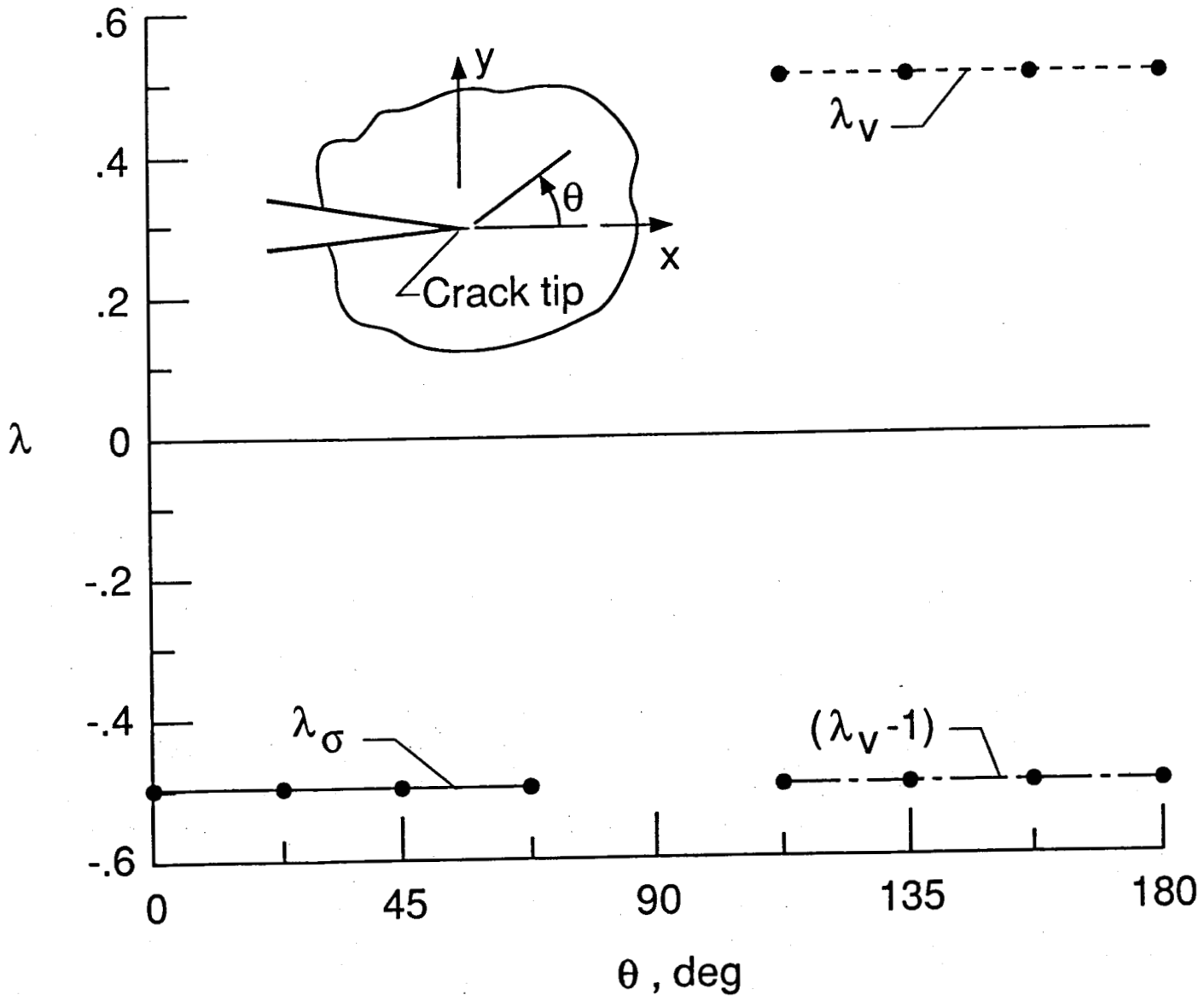

Figure 5.- Variation of λ_σ and λ_V for various θ for the plane-strain problem

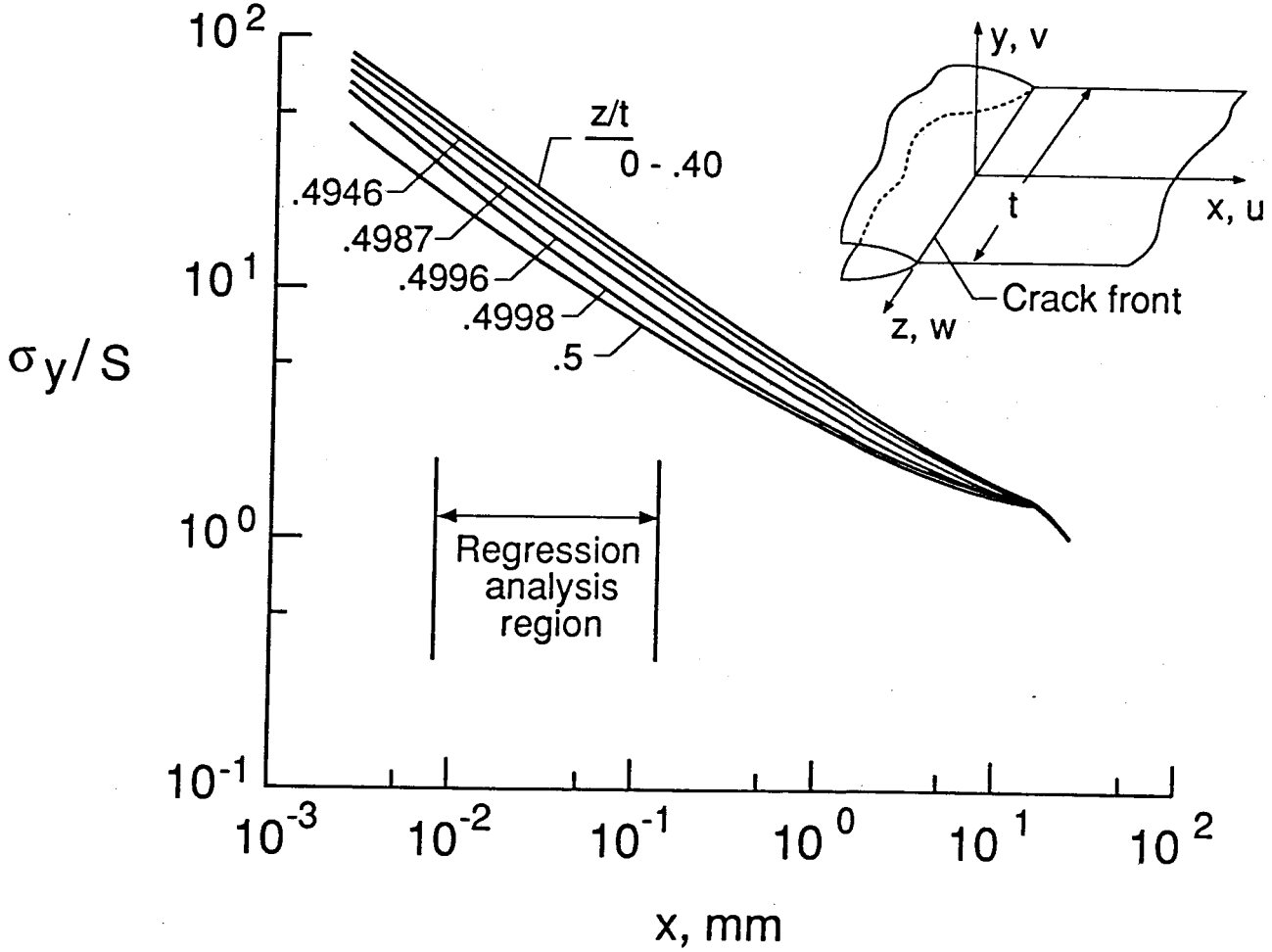

Figure 6.- Normalized λ_σ distribution ahead of the crack front at various z = constant stations from the mid-plane (ν = .3)

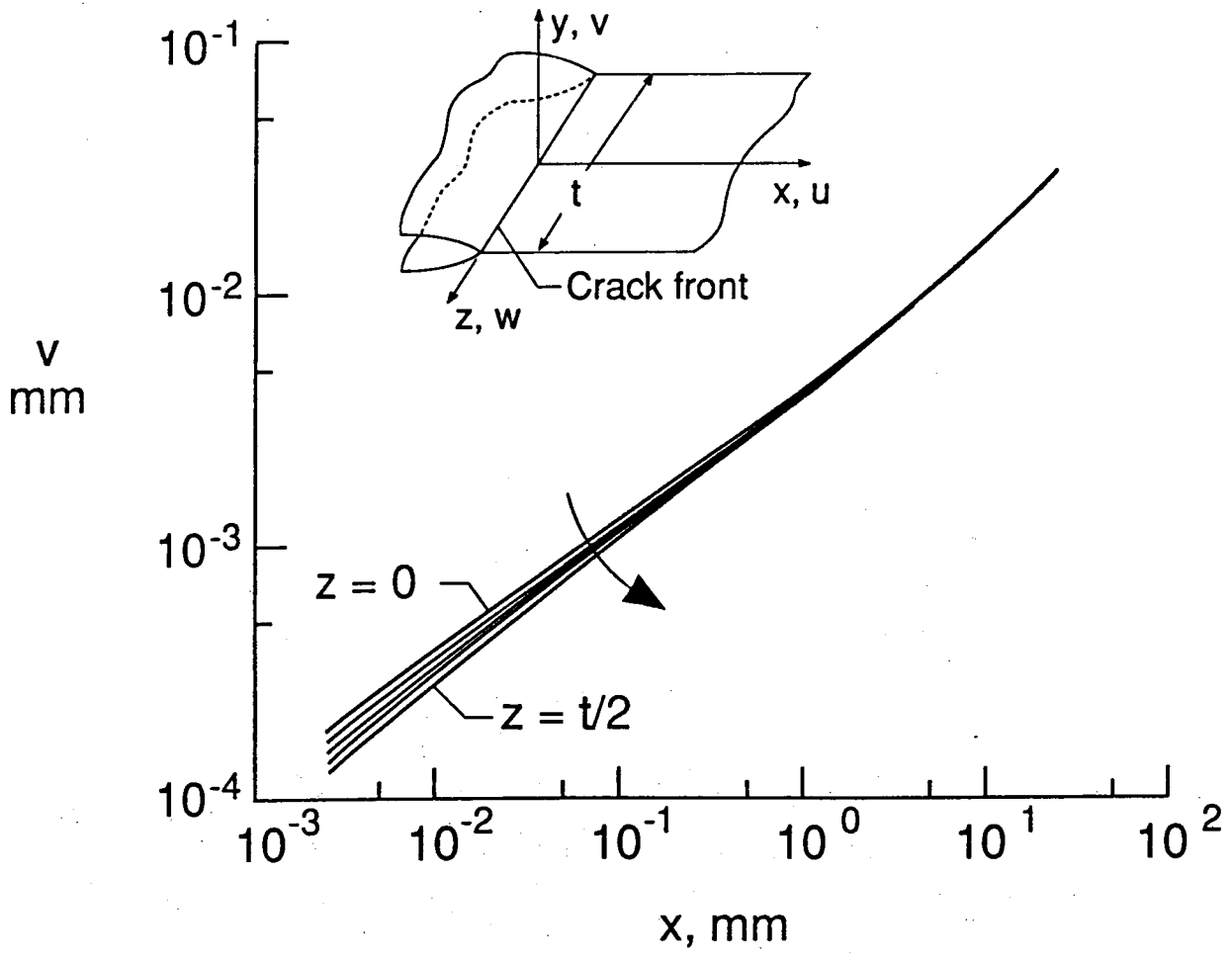

Figure 7.- Opening displacement distribution behind the crack front at various z = constant stations from the mid-plane (ν = .3)

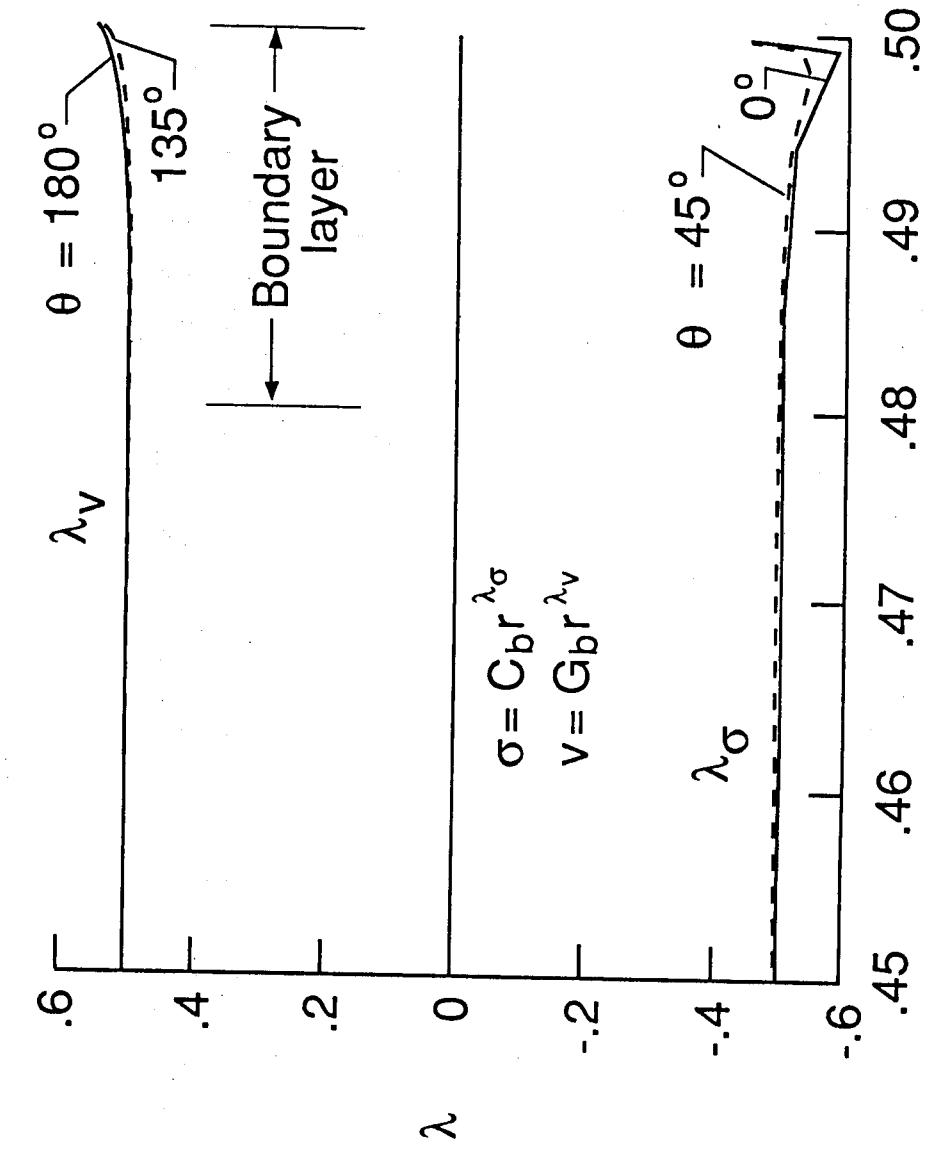

Figure 8.- Variation of λ_σ and λ_v along the crack front

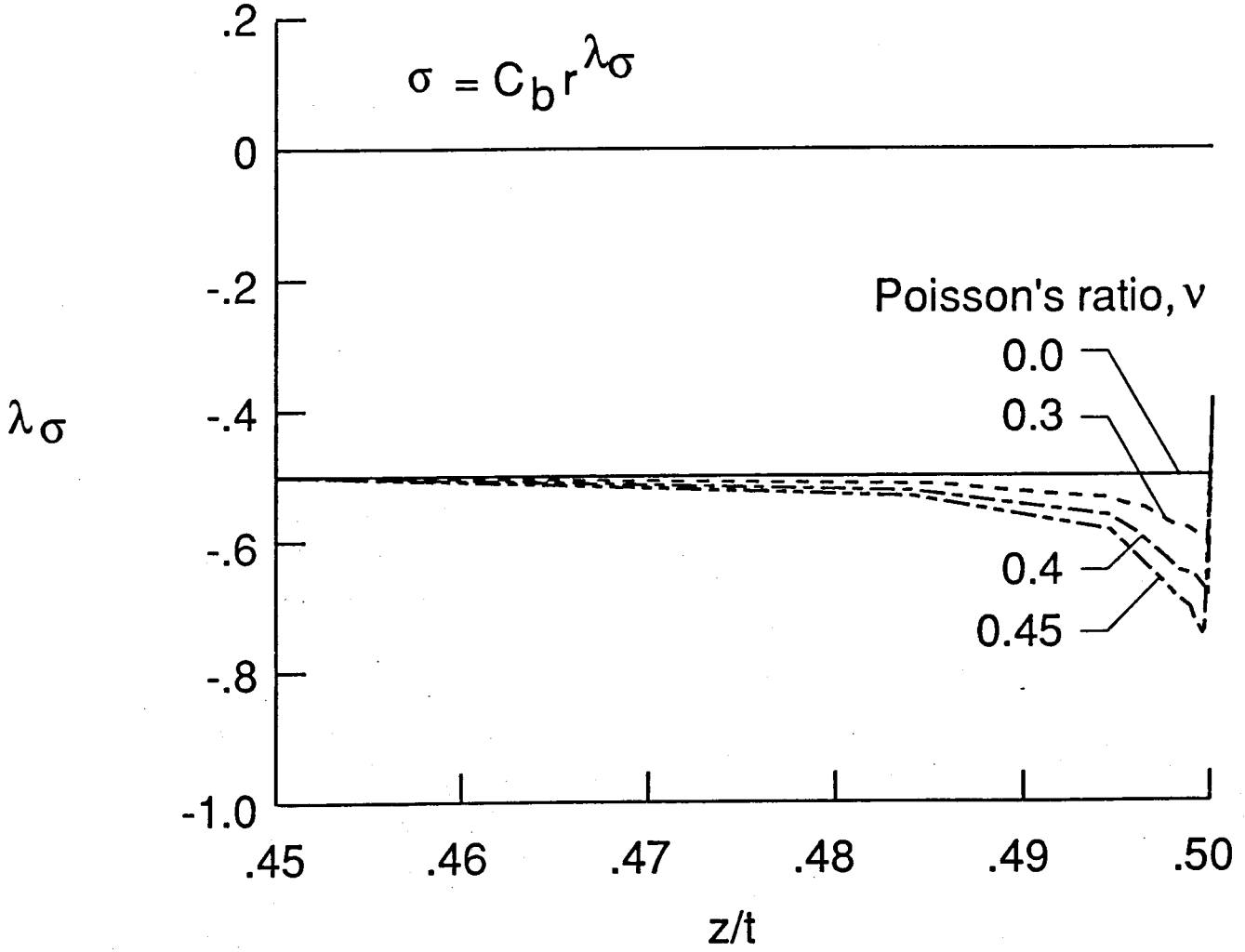

Figure 9.- Variation of λ_σ (Eq. 12) for various values of Poisson's ratio

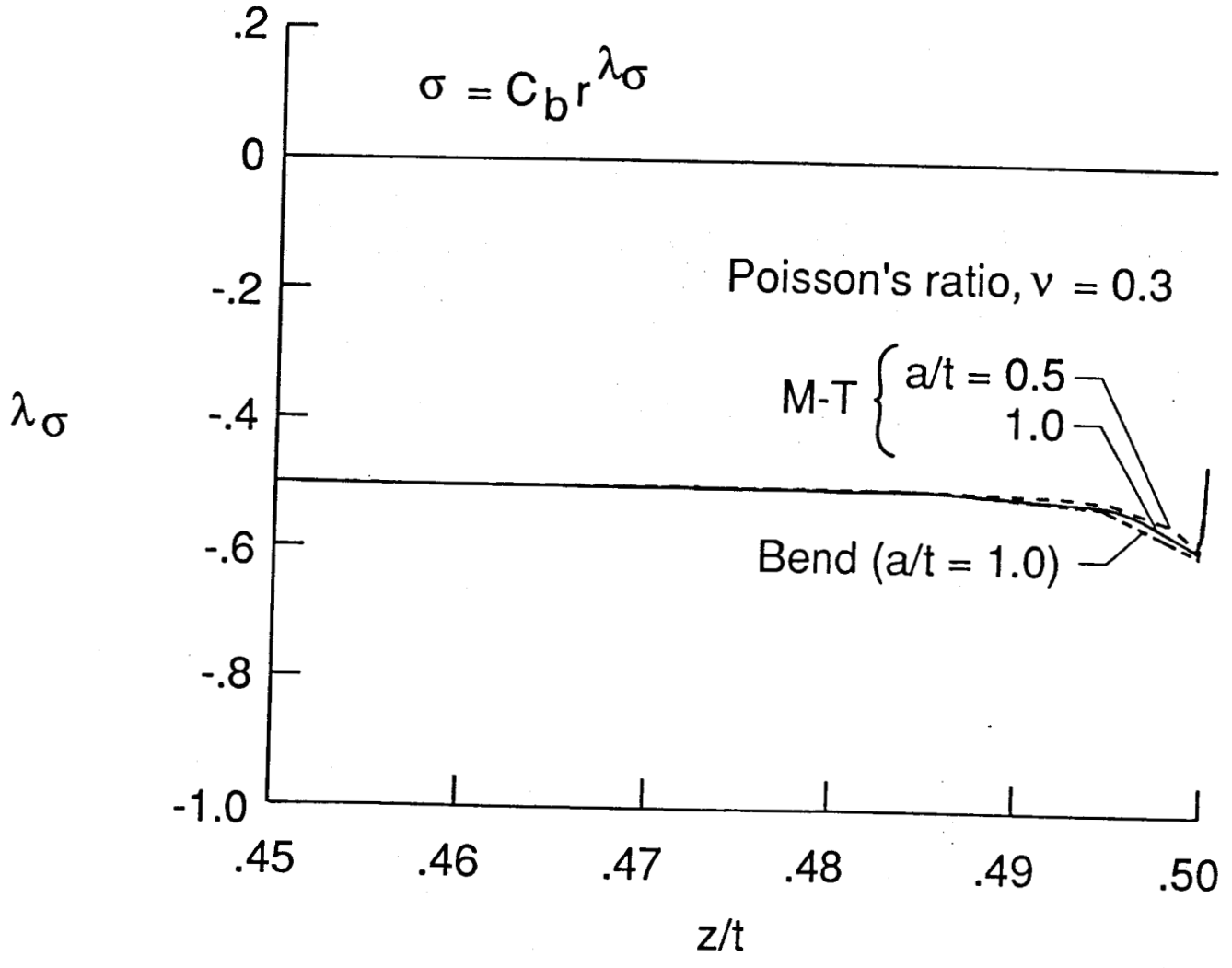

Figure 10.- Variation of λ_σ (Eq. 12) along the crack front for M-T and bend specimens

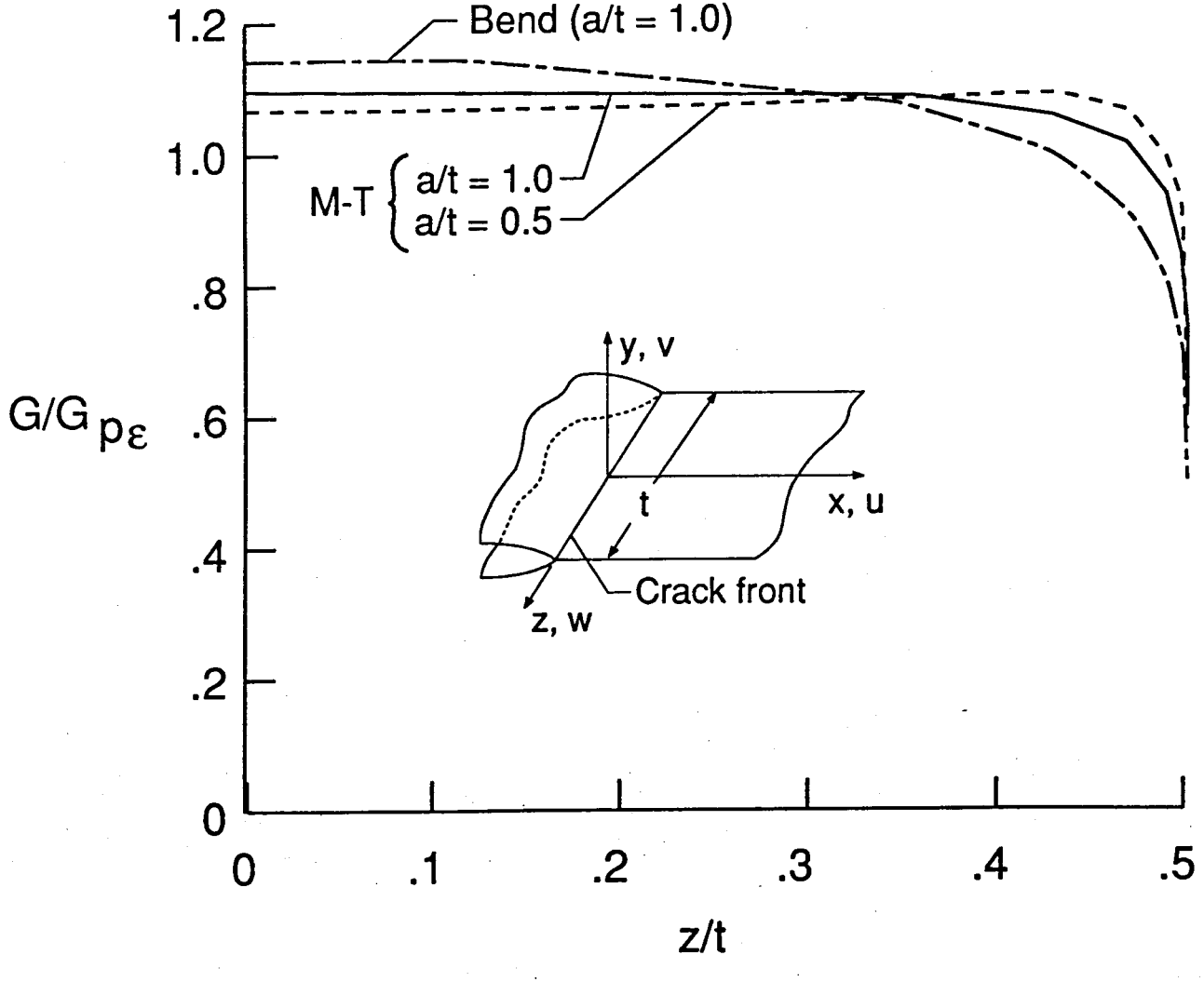

Figure 11.- Variation of normalized G along the crack front for M-T and bend specimens

NASA

Report Documentation Page

1. Report No.	2. Government Accession No.	3. Recipient's Catalog No.
NASA CR-181840		

4. Title and Subtitle	5. Report Date
Treatment of Singularities in Cracked Bodies	May 1989
	6. Performing Organization Code

7. Author(s)	8. Performing Organization Report No.
K. N. Shivakumar and I. S. Raju	10. Work Unit No. 505-63-01-05

9. Performing Organization Name and Address	11. Contract or Grant No.
Analytical Services and Materials, Inc. Hampton, VA 23666	NAS1-18599
	13. Type of Report and Period Covered
12. Sponsoring Agency Name and Address	Contractor Report
National Aeronautics and Space Administration Langley Research Center Hampton, VA 23665-5225	14. Sponsoring Agency Code

15. Supplementary Notes

Langley Technical Monitor: C. A. Bigelow

16. Abstract

Three-dimensional finite-element analyses of middle-crack tension (M-T) and bend specimens subjected to mode I loadings were performed to study the stress singularity along the crack front. The specimen was modeled using 20-node isoparametric elements. The displacements and stresses from the analysis were used to estimate the power of singularities using a log-log regression analysis along the crack front. The analyses showed that finite-sized cracked bodies have two singular stress fields of the form

$\sigma = Co\ (\theta,z)\ r^{-1/2} + Do\ (\theta,\phi)\ R^{\lambda\sigma}$. The first term is the cylindrical singularity with the power -1/2 and is dominant over the middle 96% (for Poisson's ratio = 0.3) of the crack front and becomes nearly zero at the free surface. The second singularity is a vertex singularity with the vertex point located at the intersection of the crack front and the free surface. The second term is dominant at the free surface and becomes nearly zero away from the boundary layer. The thickness of the boundary layer depends on Poisson's ratio of the material and is independent of the specimen type. The thickness of the boundary layer varied from 0% to about 5% of the total specimen thickness as Poisson's ratio varied from 0.0 to 0.45.

Because there are two singular stress fields near the free surface, the strain energy release rate (G) is an appropriate parameter to measure the severity of the crack.

17. Key Words (Suggested by Author(s))	18. Distribution Statement
Boundary layer Finite-element Vertex singularity Cylindrical singularity Three-dimensional cracked body	Unclassified - Unlimited Subject Category - 39

19. Security Classif. (of this report)	20. Security Classif. (of this page)	21. No. of pages	22. Price
Unclassified	Unclassified	44	A03